3D SAR Imaging of a Forest Using Airborne MB-SAR Data at L- and P-band: Data Processing and Analysis

Othmar Frey, Erich Meier
Remote Sensing Laboratories, University of Zurich, Switzerland

Abstract

Using a time-domain back-projection based focusing algorithm in combination with three tomographic focusing techniques (multilook standard beamforming, robust Capon beamforming, and MUSIC) a 3D volume containing a forested area has been tomographically imaged at L- and P-band. In this paper, we present further results and insights obtained by processing and analyzing these data sets with respect to the localization of the scattering sources using the three different focusing techniques, as well as for both, the two frequency bands and the different polarimetric channels.

1 Introduction

Finding new ways to gain or improve the knowledge about the structure and the backscattering behavior of forests in order to finally estimate biophysical parameters using synthetic aperture radar data has become a major research topic within the SAR remote sensing community.

With prospective spaceborne SAR remote sensing missions BIOMASS and Tandem-L at P-band and L-band, respectively, these frequency bands have even gained in importance.

In September 2006, an airborne SAR campaign has been flown by the German Aerospace Center's E-SAR system over a test site in Switzerland [1], where two fully polarimetric tomographic data sets (P-band and L-band) of a partially forested area have been taken (see **Table 1** for the sensor specifications, **Table 2** contains a summary of the parameters which characterize the tomographic data sets).

Meanwhile, an analysis of the localization of the main back-scattering elements obtained by means of tomographic processing of the two (L- and P-band) airborne fully-polarimetric multibaseline SAR data sets of the forested area using three different focusing techniques—multilook standard beamforming (MLBF), robust Capon beamforming (RCB), and multiple signal classification (MUSIC)—has been carried out.

In this paper, the processing approaches are sketched and excerpts from the data analysis are presented. In particular, we have (1) included a full three-dimensional image of the forest obtained from the L-band tomographic data set and having applied the MUSIC method (see **Figure 1**) for focusing in the normal direction; (2) vertical slices through the volume are presented for the L-band case and all focusing methods employed (MLBF, RCB, and MUSIC) (see **Figure 2**); and (3) vertical profiles of the back-scattering intensity for both the P-band and the L-band data set (see **Figure 3**).

	P-band	**L-band**
Carrier frequency	350 MHz	1.3 GHz
Chirp bandwidth	70 MHz	94 MHz
Sampling rate	100 MHz	100 MHz
PRF	500 Hz	400 Hz
Ground speed	90 m/s	90 m/s

Table 1: E-SAR system specifications

	P-band	**L-band**
No. of data tracks	11+1	16+1
Nominal track spacing d_n	57 m	14 m
Horizontal baselines	40 m	10 m
Vertical baselines	40 m	10 m
Synthetic aperture in normal direction L	570 m	210 m
Nominal resolution in normal direction δ_n	3 m	2 m
Approx. unambiguous height H	30 m	30 m

Table 2: Nominal parameters of the tomographic acquisition patterns.

1.1 Baseline Calibration

In the following, the processing approach used for the baseline calibration is given. Although each data track is processed in the time domain based on the original flight path, the data is reassigned to a common azimuth direction for all flight tracks as detailed here: (1) Calculation of a linear approximation of each flight track by fitting the linear flight track model to the measured antenna positions in 3D space in a total least squares sense. (2) A common azimuth direction is then determined by averaging the direction vectors of the individual linearized flight tracks. (3) Based on the common azimuth direction the 3D reconstruction grid is built in an azimuth/ground-range/height layout. (4) Time-domain back-projection pro-

cessing of all data sets onto the 3D reconstruction grid using the 3D antenna positions. For each data point the range distance r_{DC} corresponding to the Doppler centroid frequency f_{DC} is stored. (5) Then, the 2D-focused SAR data sets are reassigned to the common azimuth direction to ensure a unified geometry and zero Doppler annotation before tomographic focusing. To this end, a phase multiply $e^{4\pi/\lambda(r_{DC}-r_{PCA})}$ is applied to each data point on the reconstruction grid, where r_{DC} is the range distance corresponding to the Doppler centroid frequency f_{DC} and where r_{PCA} is the range distance at the point of closest approach (PCA). (6) Eventually, the remaining global phase offsets between the individual tracks of the tomographic data set are removed.

2 Tomographic Focusing

A modified time-domain tomographic processing approach is pursued to obtain a three-dimensional image of a partially forested area: namely, a combination of standard TDBP processing for azimuth focusing [2] and time-domain multilook-based methods for tomographic focusing in the normal direction.

2.1 Multilook Standard Beamforming

The standard multilook beamforming approach has been applied using the time-domain back-projection based approach described in [3].

2.2 Multiple Signal Classification

In the following the main steps to compute the location of the scatterers based on MUSIC [4] is given:

1. Calculate the sample covariance matrix $\mathbf{R}$.
2. Calculate the eigen-decomposition of the sample covariance matrix
$$\mathbf{R} = \mathbf{U}\mathbf{D}\mathbf{U}^H \tag{1}$$
3. Permute the elements of the matrices such that the eigenvalues in $\mathbf{D}$ are sorted in nonincreasing order: $\gamma_1 \geq \gamma_2 \geq ... \geq \gamma_K$; the matrix of eigenvectors $\mathbf{U}$ is adjusted accordingly.
4. Set a threshold for the eigenvalue that separates the signal- and the noise-subspace, respectively.
5. Estimate the locations of the sources by evaluating
$$\hat{P}_M = \frac{1}{\mathbf{a}^H\mathbf{G}\mathbf{G}^H\mathbf{a}} \tag{2}$$
where $G = [\mathbf{u}_{p+1}...\mathbf{u}_K]$ contains the eigenvectors that span the noise space.

2.3 Robust Capon Beamforming

While the MUSIC algorithm possesses an inherent robustness against steering vector errors, as has been shown in [5], in the case of the Capon beamformer, an improved resolution and a better reduction of the side lobes can either be obtained if the steering vector is calibrated perfectly, or, if the Capon beamformer is extended in such a way that the unknown true steering vector $\mathbf{a}$ is estimated along with the power P_C. Li et al. [6] and Stoica et al. [7] have proposed such a robust version of the Capon beamformer that can still be solved in an efficient manner. Their approach has been used in this paper for robust Capon beamforming and in the following we indicate the steps to compute the robust Capon beamformer, which is found by solving the following expression [6]

$$\max_{\mathbf{a},P_C} P_C \quad \text{subject to} \quad \mathbf{R} - P_C\mathbf{a}\mathbf{a}^H \tag{3}$$

$$(\mathbf{a}-\bar{\mathbf{a}})^H\mathbf{C}^{-1}(\mathbf{a}-\bar{\mathbf{a}}) \leq 1. \tag{4}$$

Using (1) the fact that $P_C = \frac{1}{\mathbf{a}^H\mathbf{R}^{-1}\mathbf{a}}$ maximizing P_C is equivalent to minimizing $\mathbf{a}^H\mathbf{R}^{-1}\mathbf{a}$, and (2) assuming that $\mathbf{a} = 0$ is not part of the uncertainty ellipsoid — i.e. the solution to $\mathbf{a}$ will lie on the boundary of the ellipsoid — and further (3) as there is not sufficient a priori information about the variance of the individual components of the steering vector the covariance matrix $\mathbf{C}$ is set to $\mathbf{C} = \epsilon\mathbf{I}$ and the estimation problem reduces to the following quadratic problem with a quadratic equality constraint

$$\min_{\mathbf{a}} \mathbf{a}^H\mathbf{R}^{-1}\mathbf{a} \qquad \text{subject to } \|\mathbf{a}-\bar{\mathbf{a}}\|^2 = \epsilon. \tag{5}$$

The expression (5) can then be solved efficiently by using the Lagrange multiplier approach

$$F(\mathbf{a},\lambda) = \mathbf{a}^H\mathbf{R}^{-1}\mathbf{a} + \lambda\cdot\left(\|\mathbf{a}-\bar{\mathbf{a}}\|^2 - \epsilon\right). \tag{6}$$

The computation of the robust Capon beamformer consists of the following steps:

1. Determine the eigen-decomposition of the sample covariance matrix R
$$\mathbf{R} = \mathbf{U}\mathbf{D}\mathbf{U}^H \tag{7}$$
and set
$$\mathbf{b} = \mathbf{U}^H\bar{\mathbf{a}}. \tag{8}$$
2. Solve
$$\sum_{m=1}^{K} \frac{|b_m|^2}{(1+\lambda\gamma_m)^2} = \epsilon \tag{9}$$
for the Lagrange multiplier λ, given the fact, that there is a unique solution in the interval $[\lambda_{low}, \lambda_{up}]$ [see [8]], where
$$\lambda_{low} = \frac{\|\bar{\mathbf{a}}\| - \sqrt{\epsilon}}{\gamma_1\sqrt{\epsilon}} \tag{10}$$
$$\lambda_{up} = \frac{\|\bar{\mathbf{a}}\| - \sqrt{\epsilon}}{\gamma_K\sqrt{\epsilon}} \tag{11}$$

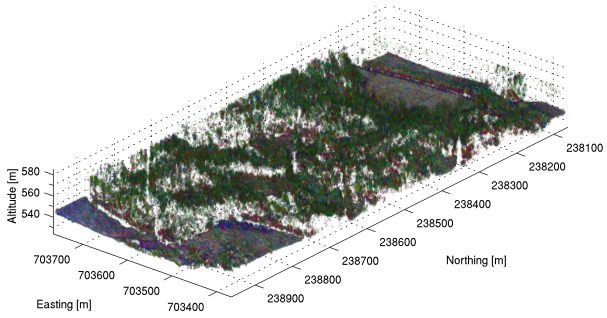

Figure 1: Tomographic image (3D voxel plot) of a partially forested area obtained from combined TDBP and MUSIC beamforming of polarimetric airborne repeat-pass multibaseline SAR data at L-band. Each channel has been scaled individually. Red (HH), green (HV), blue (VV). Low intensity = high transparency of the voxel.

3. Calculate an estimate $\hat{\mathbf{a}}$ of the unknown steering vector $\mathbf{a}$

$$\hat{\mathbf{a}} = \bar{\mathbf{a}} - \mathbf{U}(\mathbf{I} + \lambda\mathbf{D})^{-1}\mathbf{b}. \tag{12}$$

4. Using the knowledge that the true steering vector $\mathbf{a}$ satisfies the condition $\mathbf{a}^H\mathbf{a} = K$ the estimated power finally yields [8]

$$\hat{P}_C = \frac{\hat{\mathbf{a}}^H\hat{\mathbf{a}}}{K\hat{\mathbf{a}}^H\mathbf{U}\boldsymbol{\Gamma}^{-1}\mathbf{U}^H\hat{\mathbf{a}}}. \tag{13}$$

The term $\frac{\hat{\mathbf{a}}^H\hat{\mathbf{a}}}{K}$ is necessary to get rid of a scaling ambiguity in the signal covariance term $P_C\mathbf{a}\mathbf{a}^H$ of (3) in the sense that each pair $P_C/\mu, \sqrt{\mu}\mathbf{a}$, for any $\mu > 0$, yields the same covariance term [8].

3 Results

In **Figure 1**, a full three-dimensional voxel image of the forest is shown, obtained by focusing the L-band tomographic data set by means of the MUSIC beamformer. **Figure 2** contains vertical slices through the volume for the L-band case and all focusing methods employed (MLBF, RCB, and MUSIC). In addition, the tomographic slices are overlaid by a DEM and a DSM created from airborne laser scanning data (TopoSys GmbH). In **Figure 3**, vertical profiles of relative intensities obtained by averaging the focused tomographic data over a circular sample plot of 300m^2 are depicted. Profile plots are given for the polarimetric channels HH, HV, and VV, for the three beamforming techniques used for focusing in the normal direction, MLBF, RCB, and MUSIC, as well as for the Pauli basis.

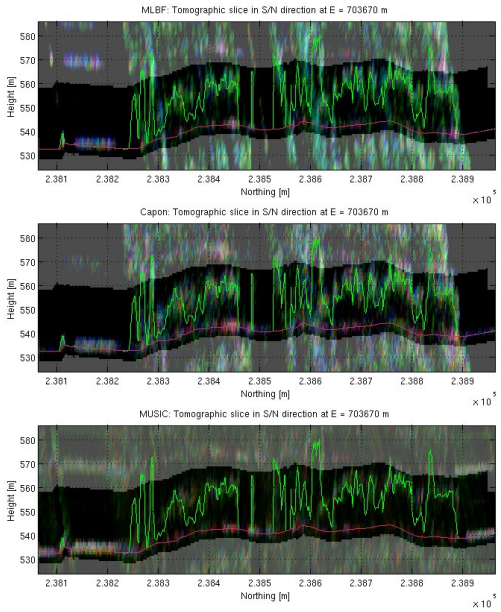

Figure 2: Vertical slices through a 3D volume of a forested area obtained from a polarimetric multibaseline L-Band data set using all (16) data tracks. Red (HH), green (HV), blue (VV). Each channel has been scaled individually. Grayed areas indicate ambiguous target regions. The tomographic slices run in south-northern direction (at easting coordinate E = 703670 m) and are overlaid by a DEM (solid red line) and a DSM (solid green line) from ALS. Top: MLBF, middle: RCB, bottom: MUSIC.

4 Discussion

We have successfully focused tomographic 3D images of a forested area (400 m x 900 m) obtained from airborne multibaseline SAR data at L- and P-band using three techniques, (1) multilook beamforming, (2) robust Capon beamforming, and (3) MUSIC for the focusing in the normal direction. Excerpts of a detailed analysis of the focused 3D SAR data sets are presented: examples of the tomographic data at L-band and profiles of normalized intensities for both L- and P-band data and for the different processing techniques have been shown. The tomographic 3D voxel image of the forested area features an unprecedented level of detail (see **Figure 1**). For instance, gaps in the canopy due to features like small forest roads of a width of a few meters only are clearly visible at the given ground range/azimuth resolution. Further, it can be stated that at L-band both, the canopy layer and the ground level are detected (see **Figures 2 & 3**).

At P-band, back-scattering from the crown layer occurs only sparsely compared to the L-band data. On the other hand, the ground level is virtually continuously detected at P-band indicating a high level of foliage-penetration.

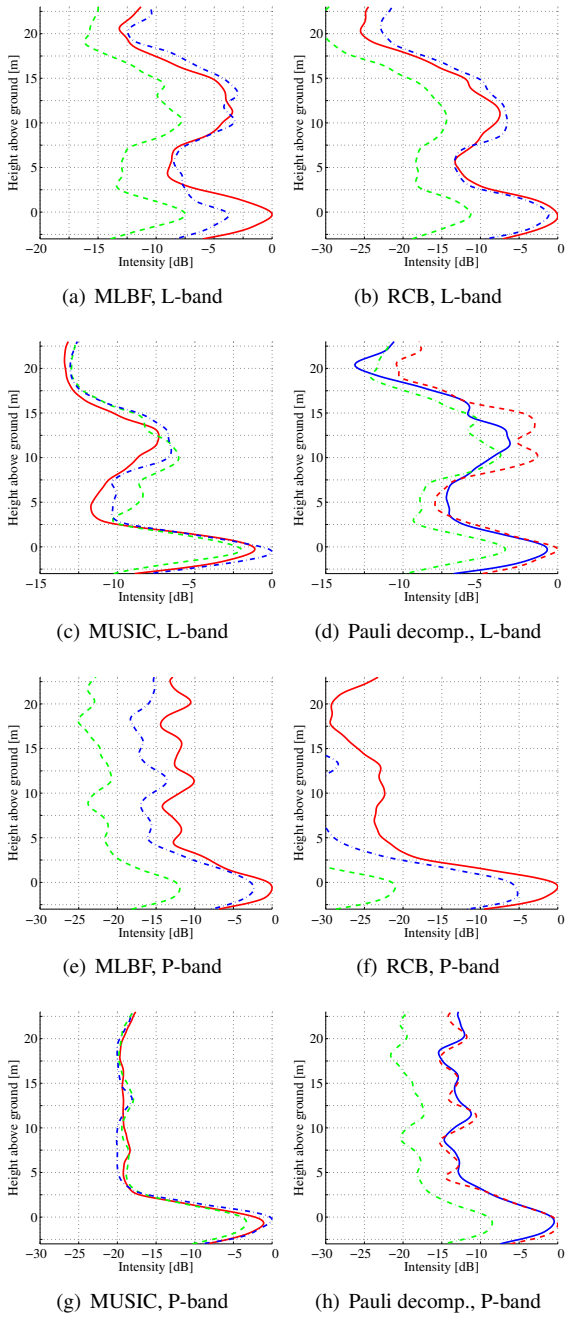

(a) MLBF, L-band (b) RCB, L-band

(c) MUSIC, L-band (d) Pauli decomp., L-band

(e) MLBF, P-band (f) RCB, P-band

(g) MUSIC, P-band (h) Pauli decomp., P-band

Figure 3: Vertical profiles of relative intensities from L- and P-band tomographic data averaged over a circular sample plot of 300m^2 for the polarimetric channels HH (—), HV (– –), and VV (·–), MLBF, RCB, and MUSIC, as well as the Pauli-basis HH+VV (—), HH-VV (– –), and 2*HV (·–) obtained from MLBF.

Somewhat unexpectedly, at P-band, the main scattering within the forest occurs at the ground level not only in the HH and VV channels but also in the HV and VH channels. The same behavior was also observed by Tebaldini et al. [9] for a different P-band data set. In conclusion, for the first time, *high-resolution tomographic* SAR data sets of *the same forested area* are available *at both, L- and P-band*, and have been analyzed in comparison with DEM/DSM reference data obtained from airborne laser scanning.

5 Acknowledgment

The authors would like to thank the E-SAR team at the Department of SAR Technology, German Aerospace Center (DLR) for their ongoing cooperation and technical support. They would also like to thank the procurement and technology center of the Swiss Federal Department of Defense (armasuisse) for funding and supporting this work.

References

[1] O. Frey, F. Morsdorf, and E. Meier, "Tomographic imaging of a forested area by airborne multi-baseline P-band SAR," *Sensors, Special Issue on Synthetic Aperture Radar*, vol. 8, no. 9, pp. 5884–5896, Sept. 2008.

[2] O. Frey, C. Magnard, M. Rüegg, and E. Meier, "Focusing of airborne synthetic aperture radar data from highly nonlinear flight tracks," *IEEE Trans. Geosci. Remote Sens.*, vol. 47, no. 6, pp. 1844–1858, June 2009.

[3] O. Frey and E. Meier, "Combining Time-Domain Back-Projection and Capon Beamforming for Tomographic SAR Processing," in *IEEE International Geoscience and Remote Sensing Symposium, IGARSS '08*, 2008, pp. 445–448.

[4] R. O. Schmidt, "Multiple emitter location and signal parameter estimation," *IEEE Transactions on Antennas and Propagation*, vol. 34, no. 3, pp. 276–280, Mar. 1986.

[5] P. Stoica, Z. Wang, and J. Li, "Extended derivations of MUSIC in the presence of steering vector errors," *IEEE Transactions on Signal Processing*, vol. 53, no. 3, pp. 1209–1211, Mar. 2005.

[6] J. Li, P. Stoica, and Z. Wang, "On robust Capon beamforming and diagonal loading," *IEEE Transactions on Signal Processing*, vol. 51, no. 7, pp. 1702–1715, 2003.

[7] P. Stoica, Z. Wang, and J. Li, "Robust Capon beamforming," *IEEE Signal Processing Letters*, vol. 10, no. 6, pp. 172–175, June 2003.

[8] P. Stoica and R. L. Moses, *Spectral Analysis of Signals*. Upper Saddle River, NJ: Prentice Hall, 2005.

[9] S. Tebaldini, F. Rocca, and A. Monti-Guarnieri, "Model based SAR tomography of forested areas," in *IEEE International Geoscience and Remote Sensing Symposium*, vol. 2, July 2008, pp. 593–596.